Contents lists available at ScienceDirect

Icarus

journal homepage: www.journals.elsevier.com/icarus

Atmospheric tides in Gale Crater, Mars

Scott D. Guzewich [a,b,*], C.E. Newman [c], M. de la Torre Juárez [d], R.J. Wilson [e], M. Lemmon [f], M.D. Smith [g], H. Kahanpää [h,i], A.-M. Harri [h], the REMS Science Team, the MSL Science Team

[a] CRESST and Planetary Systems Laboratory, NASA/GSFC, Greenbelt, MD 20771, United States
[b] Universities Space Research Association, 7178 Columbia Gateway Drive, Columbia, MD 21046, United States
[c] Ashima Research, Pasadena, CA 91106, United States
[d] Jet Propulsion Laboratory, California Institute of Technology, Pasadena, CA 91109, United States
[e] Geophysical Fluid Dynamics Laboratory, Princeton, NJ 08540, United States
[f] Texas A&M University, College Station, TX 77843, United States
[g] Planetary Systems Laboratory, NASA/GSFC, Greenbelt, MD 20771, United States
[h] Finnish Meteorological Institute, Helsinki, Finland
[i] Aalto University, Espoo, Finland

ARTICLE INFO

ABSTRACT

Atmospheric tides are the primary source of daily air pressure variation at the surface of Mars. These tides are forced by solar heating of the atmosphere and modulated by the presence of atmospheric dust, topography, and surface albedo and thermal inertia. This results in a complex mix of sun-synchronous and non-sun-synchronous tides propagating both eastward and westward around the planet in periods that are integer fractions of a solar day. The Rover Environmental Monitoring Station on board the Mars Science Laboratory has observed air pressure at a regular cadence for over 1 Mars year and here we analyze and diagnose atmospheric tides in this pressure record. The diurnal tide amplitude varies from 26 to 63 Pa with an average phase of 0424 local true solar time, while the semidiurnal tide amplitude varies from 5 to 20 Pa with an average phase of 0929. We find that both the diurnal and semidiurnal tides in Gale Crater are highly correlated to atmospheric opacity variations at a value of 0.9 and to each other at a value of 0.77, with some key exceptions occurring during regional and local dust storms. We supplement our analysis with MarsWRF general circulation modeling to examine how a local dust storm impacts the diurnal tide in its vicinity. We find that both the diurnal tide amplitude enhancement and regional coverage of notable amplitude enhancement linearly scales with the size of the local dust storm. Our results provide the first long-term record of surface pressure tides near the martian equator.

© 2015 Elsevier Inc. All rights reserved.

1. Introduction

From Mariner 9 through the Mars Reconnaissance Orbiter (MRO) and the Mars Science Laboratory (MSL), atmospheric observations of Mars have illuminated the major role of suspended mineral dust in controlling atmospheric temperatures and hence modifying the atmospheric circulation. Increased atmospheric dust opacity is responsible for producing a deeper meridional overturning circulation (Haberle et al., 1982; Wilson, 1997; Newman et al., 2002a, 2002b) and altering the phases and amplitudes of thermal tides (e.g., Leovy and Zurek, 1979). Viking lander observations of surface air pressure, atmospheric tides, and the response of those tides to varying atmospheric dust loadings has served as the foundation for much of Mars atmospheric science in the last 3 decades.

The long, multiple Mars Year (MY) duration of the Viking landers make them unique to-date. The seminal works of Leovy and Zurek (1979) and Zurek and Leovy (1981) firmly established the coupling of Mars atmospheric dynamics and dust opacity. The complexities and nuances of this coupling continue to be studied today.

The Mars Science Laboratory (MSL) Rover Environmental Monitoring System (REMS) is the most capable and longest-lived surface weather station on Mars since the Viking landers. REMS is a suite of instruments measuring temperature, pressure, wind, surface temperature, downward ultraviolet flux, and humidity (Gómez-Elvira et al., 2012) at the rover's location. The REMS dataset has already produced considerable insight into the nature of the environment in Gale Crater (e.g., Haberle et al., 2014; Harri et al., 2014; Gómez-Elvira et al., 2014; Hamilton et al., 2014; Martínez et al., 2014; Martín-Torres et al., 2015).

Unlike the Viking landers, which landed at middle northern latitudes, MSL and REMS are located very near the equator. While this

---

* Corresponding author at: Universities Space Research Association, 7178 Columbia Gateway Drive, Columbia, MD 21046, United States.

precludes REMS from observing the baroclinic traveling waves common to the higher latitudes (i.e., the familiar low- and high-pressure systems of terrestrial weather reports), daily variations in the tropical latitudes are heavily dominated by tides (Wilson and Hamilton, 1996).

Atmospheric tides are a response to the diurnal cycle of solar heating. They are manifested as planetary-scale inertia-gravity waves and are additionally modified and forced by varying surface properties (e.g., topography and thermal inertia) and atmospheric aerosol loading. Chapman and Lindzen (1970) described the formal mathematics of Laplace's Tidal Equations and their solutions (known as Hough functions). As Leovy and Zurek (1979) showed and numerous further studies have elucidated (e.g., Leovy, 1981; Wilson and Hamilton, 1996; Bridger and Murphy, 1998; Guzewich et al., 2014), the observed features of Mars atmospheric tides are closely tied to atmospheric dust loading. More recent work has shown that tides are also sensitive to water ice aerosol loading (Kleinböhl et al., 2013; Wilson and Guzewich; 2014; Wilson et al., 2014). Tides can be divided into two broad groups: migrating tides and non-migrating tides. The primary difference between these groups is that the migrating tides are westward-propagating and sun-synchronous, while the non-migrating tides can be westward- or eastward-propagating and are not sun-synchronous.

The manifestation of an individual atmospheric tide (e.g., the migrating diurnal tide) in the atmosphere is the result of the super-position of a combination of Hough function solutions, each solution having its own meridional and vertical structure. The lowest-order Hough function solution is known as the "gravest" mode. Additionally, each Hough function (due to their varying meridional and vertical structures) responds uniquely to forcing mechanisms such as the presence, horizontal and vertical extents, and opacity of atmospheric dust and water ice. For example, the gravest Hough mode of the migrating diurnal tide exhibits is equatorially-trapped (Chapman and Lindzen, 1970; Wilson and Hamilton, 1996; Guzewich et al., 2012) and thus is insensitive to dust aerosol forcing at higher latitudes. The vertical wavelength of the gravest Hough mode of the migrating diurnal tide is also relatively small (approximately 32 km) and hence is more sensitive to how dust is distributed in the vertical column. The gravest Hough mode of the migrating semidiurnal tide, however, is meridionally-broad with a very long vertical wavelength (100–200 km) and responds efficiently to global aerosol loading (e.g., Bridger and Murphy, 1998) while being relatively insensitive to local dust heating. Indeed, the amplitude of the migrating semidiurnal tide has even been used to estimate globally-averaged aerosol loading (Zurek, 1980; Zurek and Leovy, 1981; Lewis and Barker, 2005; Wilson et al., 2008). Tidal theory suggests that the properties of the migrating diurnal tide at a given surface location (i.e., REMS observing air pressure in Gale Crater) is a combination of several Hough modes while the migrating semidiurnal tide is predominantly represented by the gravest Hough mode (Chapman and Lindzen, 1970).

In this work, we present an analysis of atmospheric tides in Gale Crater, Mars, as observed by the REMS air pressure sensor. In Section 2, we discuss the REMS data and our methodology for analyzing atmospheric tides, as well as providing some background information on the MarsWRF general circulation model (GCM), which we use to contextualize and extend our data analysis. Section 3 provides the analysis of tides in REMS pressure measurements, while Section 4 links that analysis to the atmospheric aerosol opacity. Section 5 compares the observed tides in Gale Crater with analysis of MarsWRF output. Section 6 focuses on the occurrence of a local dust storm near Gale Crater, and through the aid of MarsWRF simulations, connects the atmospheric response of this storm to tidal theory. Finally, Section 7 concludes the paper.

2. Data and methodology

2.1. REMS observations

The REMS air pressure sensor is located inside the body of the Curiosity rover and can measure pressure at a cadence of 1–0.01 Hz (Gómez-Elvira et al., 2012). In typical planning for a sol of MSL operations, REMS is scheduled to conduct 5-min dura-tion "background" observations at the top of each hour (local Mars solar time, LMST) and periodic hour-long (and occasionally longer) "extended" observation blocks. The timing of these extended observations is decided according to a rotating cadence, such that all times of sol are typically observed at least once in any 6-sol per-iod (Gómez-Elvira et al., 2014). Harri et al. (2014) discusses the REMS pressure sensors in great detail and preliminary interpreta-tion of the first observations by these sensors was described by Haberle et al. (2014). The reader is referred to the above works for in-depth discussion of the workings of the REMS pressure sensors. In the frequency range (diurnal through quadiurnal) discussed in this study the most significant error mode is the tem-perature hysteresis that causes <±0.75 Pa "repeatability variation" (Harri et al., 2014). Even if the magnitude of this artificial signal is sometimes proportional to the amplitudes of the terdiurnal and quadiurnal tides (Section 3), it has been shown that even in the worst case it has practically no effect on the amplitudes (<0.25 Pa uncertainty) and phases (phase variations typically of <5 min) of the four first harmonics of the daily pressure variation (H. Kahanpää, REMS Team Meeting, May 20, 2014). These uncer-tainties are significantly lower than the 8 Pa discretization error in Viking data (e.g., Tillman et al., 1993). Thus, we ignore the instrument uncertainty factors for the remainder of this discussion.

In this paper we use the time convention of areocentric solar longitude (shortened to "L_s") and the Mars Year notation of Clancy et al. (2000) which defines $L_s = 0°$ of Mars Year 0 (MY0) on April 11th, 1955. $L_s = 0°$ of a given Mars Year occurs at northern hemisphere spring equinox. Note for reference that times can be indexed by "MSL Year", counted from MSL's landing on August 6th, 2012. Hence, MSL Year 1 runs from MY31 $L_s = 150.5°$ to MY32 $L_s = 150.5°$.

The data used in this study (version 1.0 of the REMS reduced data records) was not available in the Planetary Data System at the time of analysis, but is now available at http://atmos.nmsu.edu/PDS/data/mslrem_1001/.

2.2. Tide analysis

The REMS background cadence ensures that pressure is always measured over the first 5 min of every hour. These regular observa-tions are most useful for analyzing atmospheric tides. For each hour, we average the pressure measurements for those first 5 min, to produce 24 data points for a given sol. We then perform a Fourier transform on this time sequence of air pressure (for each individual sol) to obtain the amplitudes and phases of each individ-ual tide frequency. We refer to these frequencies as "diurnal" (once-per-sol), "semidiurnal" (twice-per-sol), "terdiurnal" (thrice-per-sol), and "quadiurnal" (four-times-per-sol). At a given single-station observing point, the time sequence of air pressure can be represented as the sum of a harmonic series of components, each with a frequency that is an integer fraction of a solar day:

$$S(p) = \sum_n s_n(p)$$

where $S(p)$ represents air pressure and n represents each individual harmonic component. Furthermore, we assume that each compo-nent can be represented as:

$$s_n(p) = s_n \sin(nt + \sigma_n)$$

where s_n represents the amplitude of the individual harmonic component, t is local true solar time (LTST) and σ represents the phase of the component. Given that REMS background observations are scheduled at the top-of-the-hour LMST, a conversion to LTST using Mars' equation of time must be performed as well (e.g. Allison and McEwen, 2000).

Without the benefit of additional meteorological stations on Mars, the migrating and non-migrating tides cannot be differentiated by REMS observations alone. From the point-of-view of a single-station observing platform, all tides of a certain frequency are aliased together; hence the observed "diurnal" tide may represent a combination of migrating and non-migrating tides with a diurnal frequency. Unfortunately, this situation will not be ameliorated by the anticipated arrival of the InSight lander in 2018, as InSight's planned landing ellipse is at nearly the same longitude as MSL (approximately 136°E vs. 137.4°E, respectively)! Hence, a GCM (with full longitude and local time resolution) is necessary to deduce what, if any, influence non-migrating tides have on the observed pressure measurements in Gale Crater.

2.3. MarsWRF introduction

MarsWRF is the Mars-specific implementation of the PlanetWRF GCM introduced by Richardson et al. (2007). MarsWRF uses a sophisticated correlated-k coefficient radiative transfer code described by Mischna et al. (2012). A variety of dust aerosol prescriptions (horizontal and vertical distributions of dust optical depth) can be applied in MarsWRF. These various dust aerosol prescriptions, with varying seasonality and magnitude of dust opacity, produce differences in the properties of the atmospheric circulation and atmospheric tides and are used to help diagnose those changes and relate them to atmospheric observations (e.g., Guzewich et al., 2013). To produce the results shown in this paper we used the "MGS Scenario" of the Mars Climate Database (Montmessin et al., 2004; Toigo et al., 2012) in addition to some uniquely-constructed idealized dust scenarios. All simulations incorporated a modified Conrath-ν vertical dust profile (Montmessin et al., 2004). MarsWRF has an inherent capability to "nest" higher-resolution mesoscale domains inside the lower-resolution global domain and we make use of this capability in this paper in an effort to capture the mesoscale features of Gale Crater. All simulations use 52 vertical levels (sigma levels) and are run for 2 Mars years, with the first year discarded as a "spin-up" year in which the modeled circulation is being established. Model data is archived at 2-h intervals, suitable for a complete tide analysis.

In Section 5, we utilize a $2° \times 2°$ horizontal resolution simulation ("standard" simulation as described by Toigo et al. (2012)) and an identical simulation with a series of mesoscale nested domains centered over Gale Crater with the highest resolution nested domain having a horizontal resolution of $0.025° \times 0.025°$ (approximately 1.5 km × 1.5 km). In Section 6, we examine a series of $5° \times 5°$ horizontal resolution simulations with unique dust aerosol prescriptions.

3. REMS pressure tide analysis

We focus our attention on the four lowest-order tide frequencies (i.e., diurnal, semidiurnal, terdiurnal, and quadiurnal) as higher-order frequencies exhibit very low amplitudes. The four tide frequencies analyzed show a great deal of variation in amplitude over the first 875 sols of the MSL mission (Fig. 1). The diurnal tide amplitude varies from a minimum of 26 Pa at MY32 L_s = 130° to a maximum of 63 Pa at MY31 L_s = 315°. The semidiurnal tide amplitude pattern mimics that of the diurnal tide to a great extent

(correlation of 0.775), but with lesser amplitudes varying from 5 Pa at MY32 L_s = 90° to 20 Pa at MY31 L_s = 210°. The terdiurnal and quadiurnal tide components are both weak, as Haberle et al. (2014) noted, and have amplitudes of generally <5 Pa. The terdiurnal and quadiurnal tides are largely anti-correlated in amplitude. These diurnal tide amplitudes range from 3% to nearly 8% of daily average surface pressure, while the semidiurnal tide amplitude is 1–2.5% and the terdiurnal and quadiurnal amplitudes are both less than 1% (not shown).

A background seasonal cycle is clearly present in both the diurnal and semidiurnal tide (compare their amplitude patterns at MY31 L_s = 200–280° and MY32 L_s = 200–280°). A well-defined seasonal cycle of tide amplitude is also evident in the Viking 1 Lander record (Wilson and Hamilton, 1996). Superimposed on this seasonal cycle are excursions associated with large dust opacity increases in the area (see Section 4). Most notable are the large regional southern hemisphere dust storm that started near MY31 L_s = 200–210°, not long after MSL landed in Gale Crater (Malin et al., 2012), a series of large "flushing" dust events near MY31 L_s = 315° (Malin et al., 2013), and a local dust storm that occurred near Gale Crater at MY32 L_s = 260° (Malin et al., 2015). These three storms correspond to the three periods with the highest diurnal tide amplitude, but such a correlation is not generally as strong for the semidiurnal tide as it is more sensitive to global versus regional or local atmospheric aerosol loading (see Sections 4 and 6). The exception is the MY31 L_s = 200° storm, which was the most spatially extended of the three increased dust events, and produced a maximum in the semidiurnal tide amplitude.

The phases of the diurnal, semidiurnal and quadiurnal tides are largely uniform throughout the observation period with mean values of 0424 h, 0929 h and 0151 h, respectively (Fig. 2). Variations around this mean are generally ±1 h, with only a handful of exceptions. The terdiurnal tide phase is much more variable, with a suggestion of a seasonal cycle to its phase changes with a phase minimum near L_s = 270°.

The most sudden phase excursions of the diurnal tide occurred during the MY31 L_s = 200–210° dust storm and again at MY32 L_s = 220°, where the diurnal tide phase briefly moved to 0230–0300 h. The similar timing of these two phase excursions in each year suggests that this may be a seasonal event. The L_s = 200–220° time period is associated with the annual increase in pre-solstice flushing dust storms where northern hemisphere frontal storms propagate dust through the Acidalia-Chryse storm track and into the southern hemisphere. In the southern hemisphere, new centers of dust lifting are often initiated. Wang et al. (2003) found that the propagation of these flushing dust storms into the southern hemisphere is dependent upon local time and hence upon whether the direction of the meridional wind associated with the diurnal tide will positively or negatively interact with the net southward motion of the dust storm. Hence, this diurnal tide phase excursion associated with flushing dust storms may act as a short-lived feedback mechanism.

4. Link with atmospheric opacity

The link between atmospheric opacity and diurnal and semidiurnal tide amplitude is obvious even by eye when comparing the MSL-observed record of atmospheric opacity (e.g., Haberle et al., 2014) and the REMS tidal amplitudes of Fig. 1. Lemmon et al. (2015) describes the method to retrieve opacities from Mars Exploration Rover Pancam images, and the method to retrieve the MastCam opacities is nearly identical. Zurek and Leovy (1981) and Bridger and Murphy (1998) (among others) have noted the strong correlation between atmospheric opacity and tide amplitudes, so we expect tide amplitudes in Gale Crater to be similarly linked to
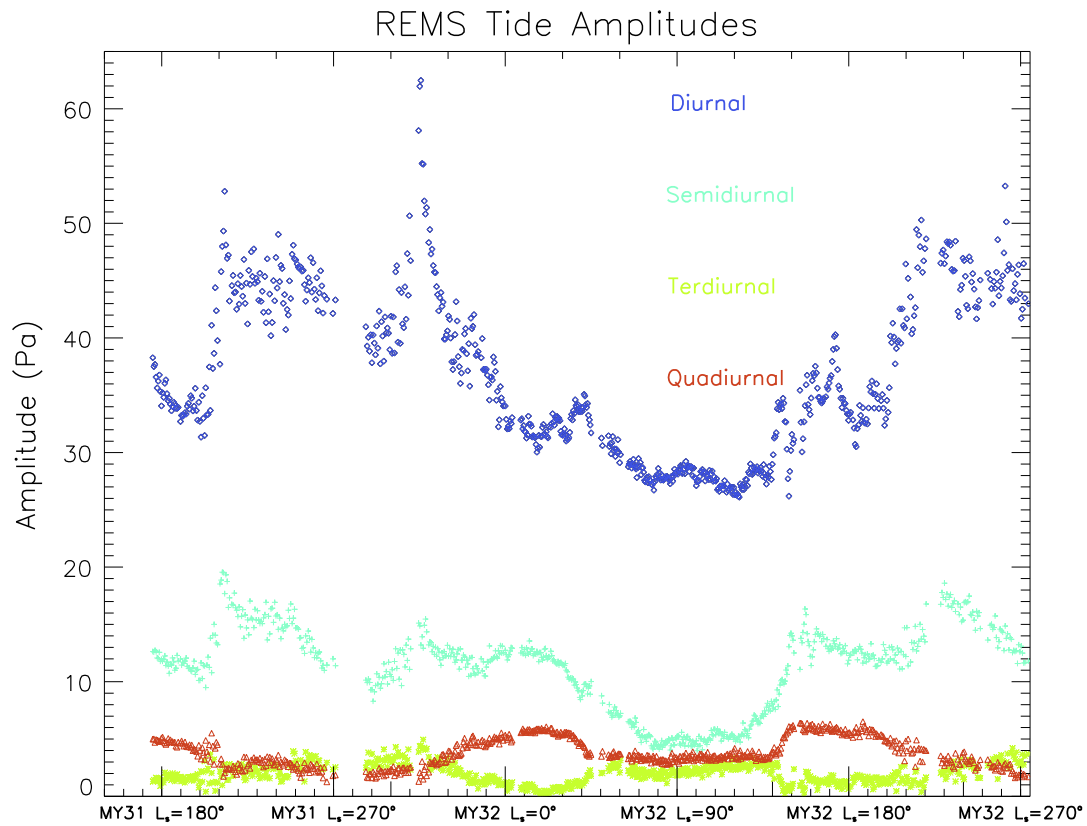
REMS Tide Amplitudes

Fig. 1. REMS diurnal (blue), semidiurnal (light blue), terdiurnal (green) and quadiurnal (orange) tide amplitudes in Pa (top) and normalized percent of daily mean pressure (bottom) over MY31–32. (For interpretation of the references to color in this figure legend, the reader is referred to the web version of this article.)
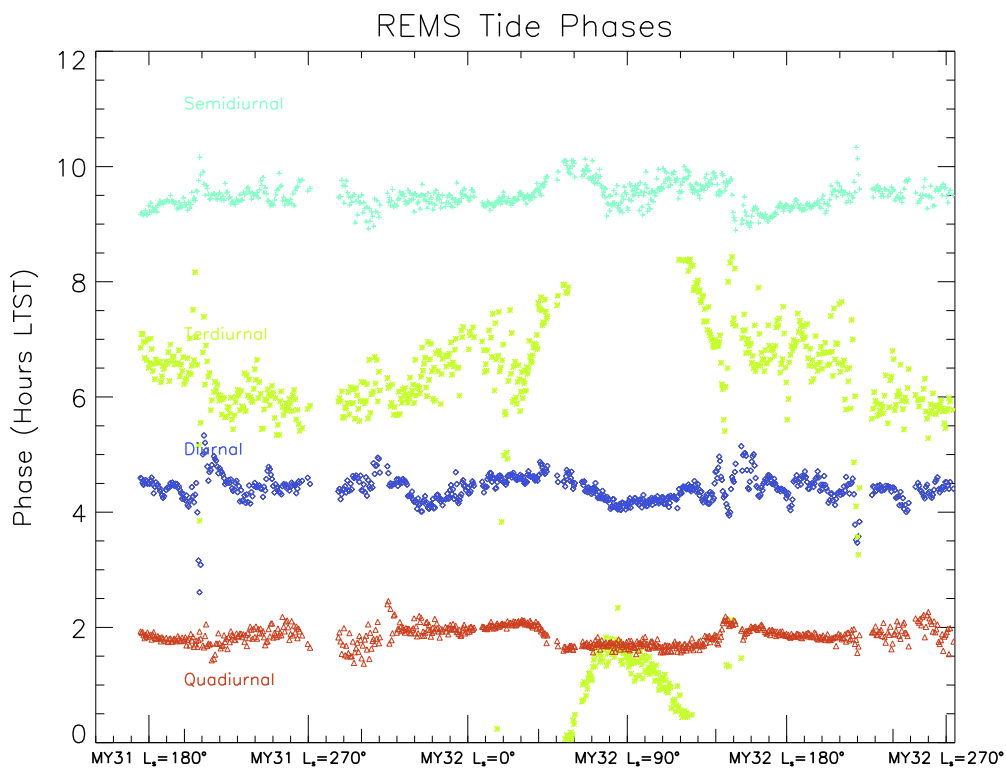
REMS Tide Phases

Fig. 2. REMS diurnal (blue), semidiurnal (light blue), terdiurnal (green) and quadiurnal (orange) tide phases in hours local true solar time over MY31–32. (For interpretation of the references to color in this figure legend, the reader is referred to the web version of this article.)

opacity. As introduced in Section 1, the precise magnitude and spatial distribution of dust opacity can produce unique responses to particular tides. In Fig. 3, we overlay the diurnal and semidiurnal tidal amplitudes with the record of MastCam 880 nm atmospheric opacity. In both cases, the tide amplitude closely tracks with the local atmospheric opacity, with a few notable exceptions.

Fig. 4 shows the correlation of the MastCam opacity record with the tide amplitudes and quantitatively confirms what is suggested visually. The diurnal and semidiurnal tide are correlated at a level of ~0.9 with MastCam opacity, indicating a very strong relationship between atmospheric aerosol loading and tide amplitude. Given how the diurnal tide is more sensitive to tropical (as well as local and regional) dust-loading, while the semidiurnal tide is more sensitive to globally-averaged aerosol loading, the close correspondence between their respective correlations indicates that the atmospheric opacity at Gale Crater is largely representative of globally-averaged atmospheric dust opacity (with some exceptions to this general rule discussed below). The higher order tide frequencies, the terdiurnal and quadiurnal tides, have almost zero correlation and a modest anti-correlation, respectively. The MarsWRF simulations also show a low correlation of dust opacity to terdiurnal and quadiurnal tide amplitudes.

The Thermal Imaging Spectrometer (THEMIS) on board the Odyssey spacecraft has created a long record of global atmospheric opacity (e.g., Smith et al., 2003) that we utilize to provide a more global perspective on atmospheric opacity during the MSL mission. Due to its orbital geometry and instrument characteristics, THEMIS is unable to observe atmospheric opacity for all latitudes at any given season, so we caveat our analysis with this known bias. Despite that, as Fig. 4 indicates, the THEMIS opacity record strongly corroborates the high correlation between atmospheric opacity and tide amplitude in Gale Crater, but at slightly lower values of ~0.65. Again the correlation values for the diurnal and semidiurnal tides are similar, corroborating that local dust opacities within Gale Crater are largely representative of the global average. We attribute the slightly lower correlation to THEMIS observations to the globally incomplete record of opacity from THEMIS due to the aforementioned bias. Outside of occasional local dust storms,

the mid- and high-latitude locations are the preferred locations for storm-scale dust lifting on Mars (Guzewich et al., 2015), thus Gale Crater is not expected to experience significant nearby dust lifting activity due to strong winds. Dust devils are a significant source of local dust lifting in the tropics. However, no dust devil streaks or direct observations of dust devils have been observed in Gale Crater from space (Moores et al., 2015), and while convective vortices are regularly measured by REMS (Kahanpää et al., submitted for publication) they appear to be largely dustless (Haberle et al., 2014; Moores et al., 2015).

We focus additional attention on two specific time periods where the correspondence pattern between the diurnal tide, semidiurnal tide, and MastCam opacity breaks down or exhibits unique behavior. The first such period is MY32 L_s = 150–160° and the second period is at MY32 L_s = 260°. In these two periods, the diurnal and semidiurnal tide respond differently to local and regional dust events on Mars, and thus provide a demonstration and validation of tidal theory. We devote Section 6 to discussion of the second period, when a local dust storm occurred near Gale Crater. The first period we discuss here.

As discussed in Malin et al. (2014a, 2014b, 2014c), the first period (MY32 L_s = 147–160°) saw a series of polar cap-edge storms in both the north and south hemispheres, some of which combined into regional storms in the southern hemisphere (e.g., in Terra Cimmeria), followed by a large northern hemisphere regional storm beginning at approximately MY32 L_s = 155°. Despite this, Malin et al. (2014a, 2014b, 2014c) note that only a minor amount of dust from these storms drifted over Gale Crater. This pattern is evident in the MastCam opacity record of the period, where opacity increased just prior to MY32 L_s = 150°, then immediately decreased before increasing again after MY32 L_s = 160° (Fig. 3). The REMS diurnal tide amplitude closely follows this pattern of local opacity increase, but the semidiurnal tide does not (Fig. 3). While the semidiurnal tide did initially increase directly in step with the local opacity near MY32 L_s = 158° and then decrease over the next few sols, the semidiurnal tide then increased again (by approximately 6 Pa) while the local opacity remains low. Both the diurnal and semidiurnal tides also experienced large phase excursions during
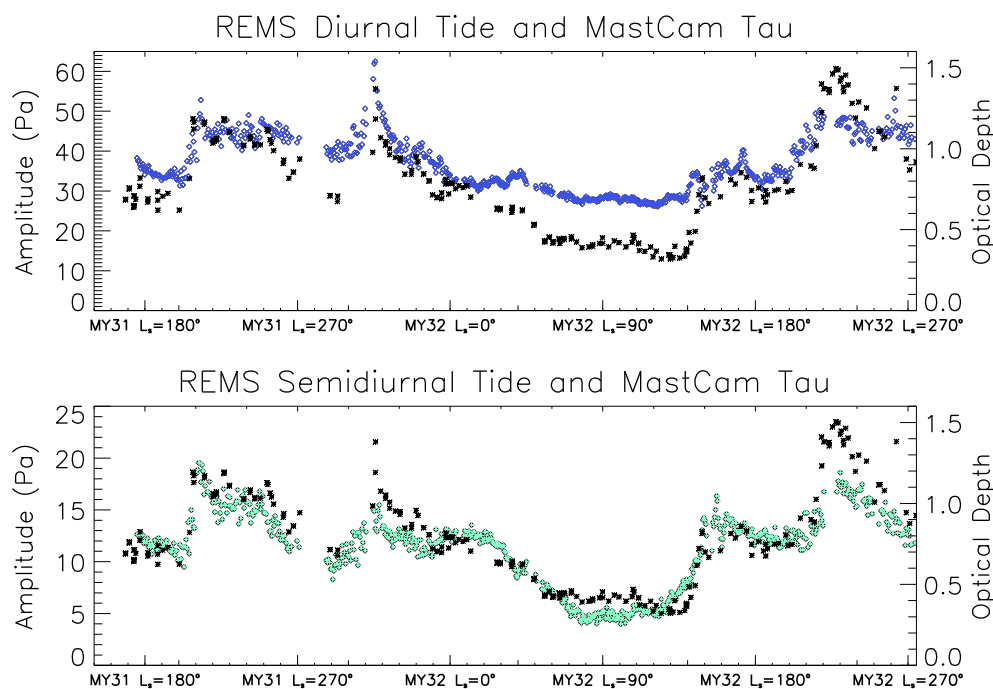

Fig. 3. REMS diurnal (top) and semidiurnal (bottom) tide amplitude over MY31–32 with MastCam 880 nm opacity overlaid.
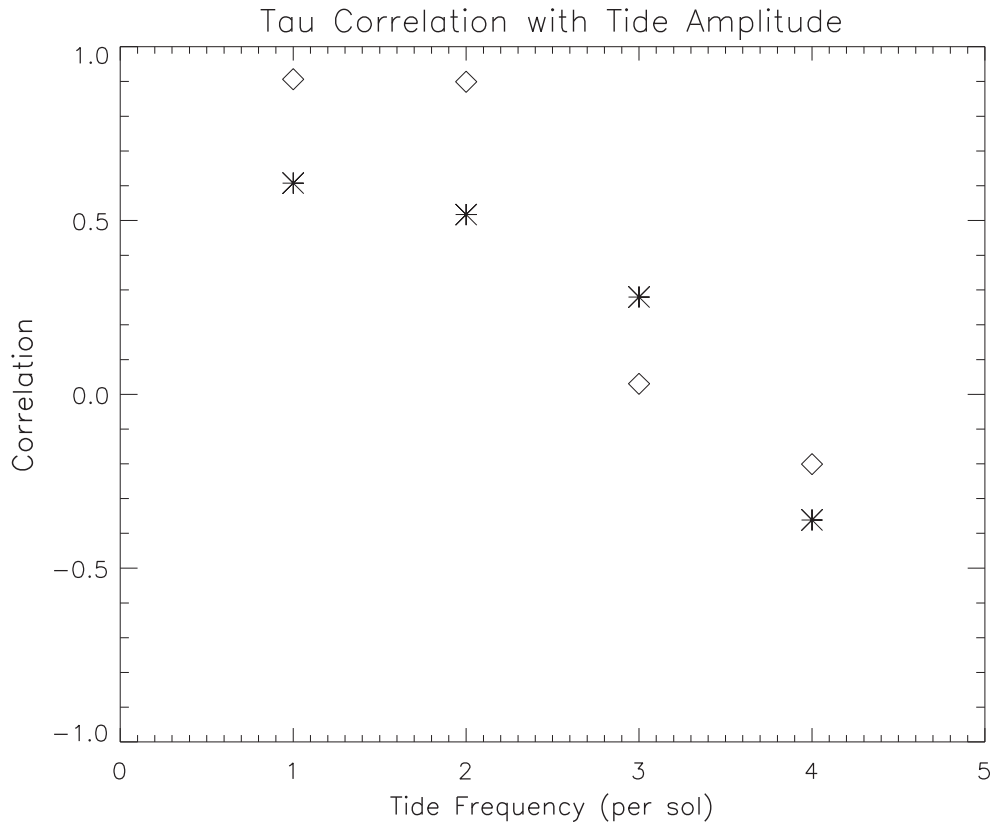
Fig. 4. Correlation of REMS tide amplitudes with MastCam 880 nm opacity (diamonds) and THEMIS dust opacity (asterisks).
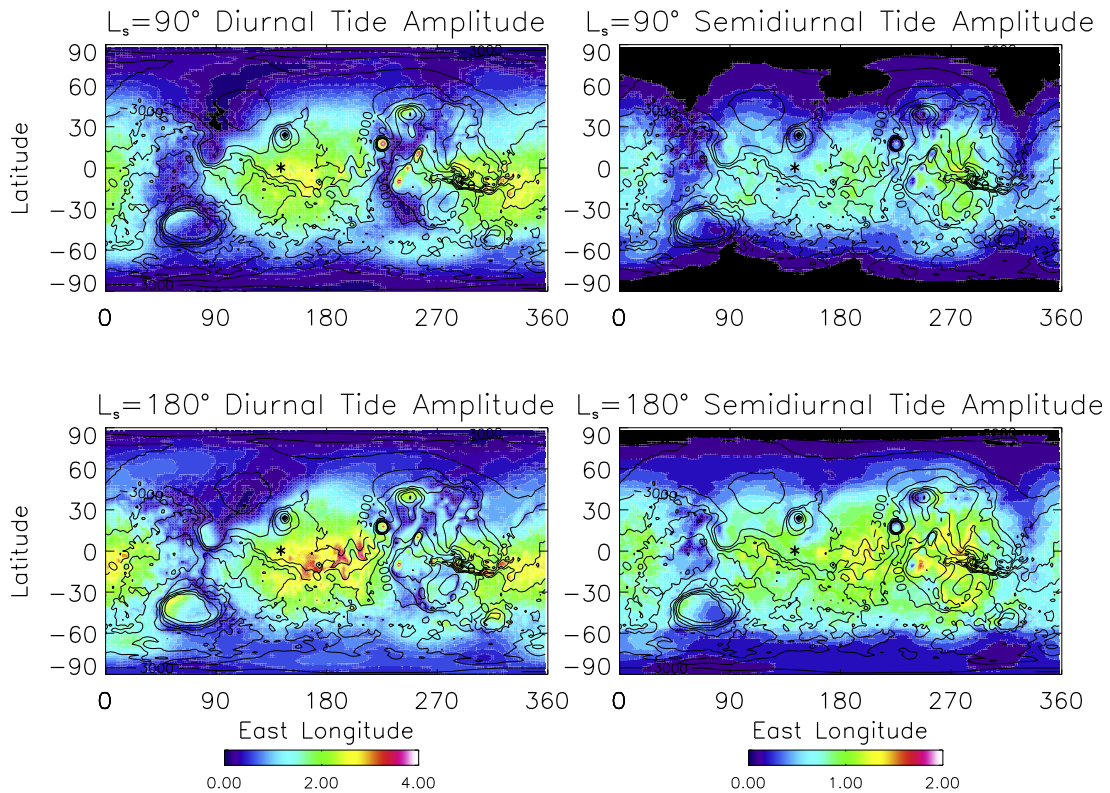

Fig. 5. Global diurnal (top) and semidiurnal (bottom) amplitude (normalized percent of local daily mean pressure) from the standard 2° × 2° MarsWRF simulation for L_s = 90° (top) and L_s = 180° (bottom). Black asterisks mark the location of Gale Crater.

this period (Fig. 2), with the semidiurnal tide phase moving nearly 1 h earlier and the diurnal tide seeing a great degree of variability (±30 min around its mean value). In this situation, the semidiurnal tide responded to globally increased opacity (likely from the large northern hemisphere regional storm that Malin et al. (2014c) note "persisted for several days" and spread dust "from Acidalia in the south to as far north as the residual polar cap"). With most of the dust lofted by this regional storm remaining confined to the northern hemisphere, the diurnal tide did not respond to this global opacity change. The gravest Hough mode of the migrating diurnal tide is equatorially-trapped and thus did not respond to dust forcing occurring north of the martian tropics while the meridionally-broad gravest Hough mode of the semidiurnal migrating tide clearly did.

Although the MastCam record of opacity cannot directly distinguish between dust and water ice opacities, the observed seasonality of opacity changes and tide variability strongly imply that dust is the major driver of tide variability at Gale Crater. Moores et al. (2015) noted that the skies above Gale are rarely cloudy, even during the aphelion cloud belt season ($\sim L_s = 40$–$140°$ in Figs. 1–3). During the aphelion cloud belt season, the diurnal and semidiurnal tide amplitudes reached their lowest points yet observed during the MSL mission. There is also little sol-to-sol variability in tide amplitude as is seen in dustier times of year. The semidiurnal tide, which is known to be an excellent diagnostic of global atmospheric aerosol loading (see Section 1 and above), exhibited a steady decline in amplitude from MY32 $L_s = 20$–$80°$. Water ice clouds

are increasing at this time of year (e.g., Smith, 2004), but dust storm activity decreases (Guzewich et al., 2015). The greatest excursions to both the tide amplitudes and phases from their mean values also occur during known dust events as observed by MARCI (Malin et al., 2012, 2013, 2014a, 2014b, 2014c, 2015).

5. GCM tide analysis

By definition, a single-station observing platform cannot distinguish between eastward- and westward-propagating tide components. Hence in this work we have thus far taken care to only refer to the "diurnal" or "semidiurnal" tides rather than the "*migrating* diurnal" or "*migrating* semidiurnal" tides. With the aid of the MarsWRF GCM, we can differentiate the individual tide components and attempt to interpret the signal being observed by REMS in Gale Crater. Our analysis technique for extracting tide amplitudes and phases at a single grid point in the MarsWRF simulations is identical to that used with REMS except using the GCM in lieu of the REMS data. The GCM allows evaluation of global maps of tide amplitude. In addition, the global coverage allows us to decompose these fields into westward- and eastward-propagating waves, for each zonal wavenumber and temporal harmonic.

In Fig. 5, we present contoured maps of diurnal and semidiurnal tide amplitudes at each individual grid point from a "standard" MarsWRF simulation at $2° \times 2°$ resolution using the Mars Climate
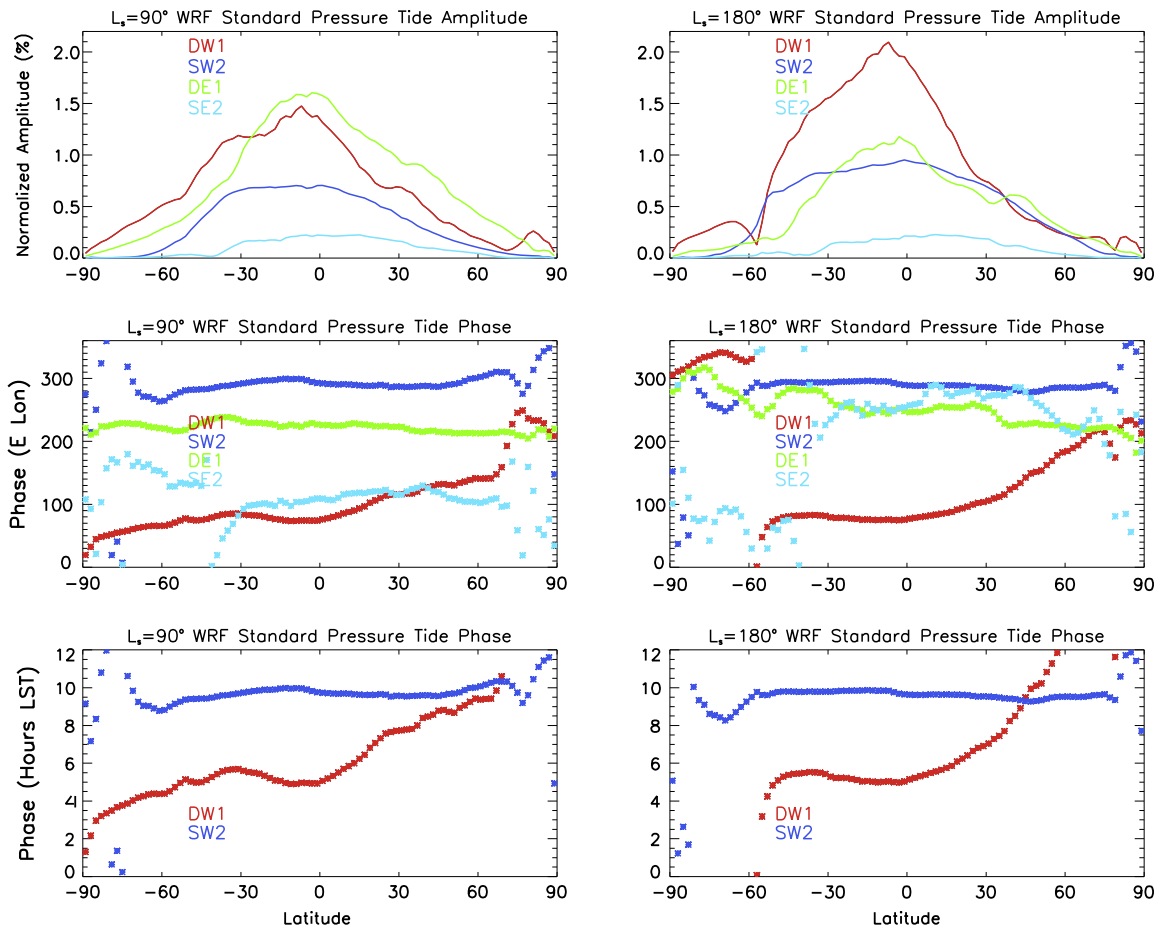

Fig. 6. Annual-average tide normalized amplitude (%, top), phase (degrees east longitude, middle), and phase (hours local true solar time, bottom) as a function of latitude for the migrating diurnal tide (DW1, red), migrating semidiurnal tide (SW2, dark blue), diurnal Kelvin wave (DE1, green), and semidiurnal Kelvin wave (SE2, light blue) from the standard $2° \times 2°$ MarsWRF simulation for $L_s = 90°$ (left) and $L_s = 180°$ (right). (For interpretation of the references to color in this figure legend, the reader is referred to the web version of this article.)
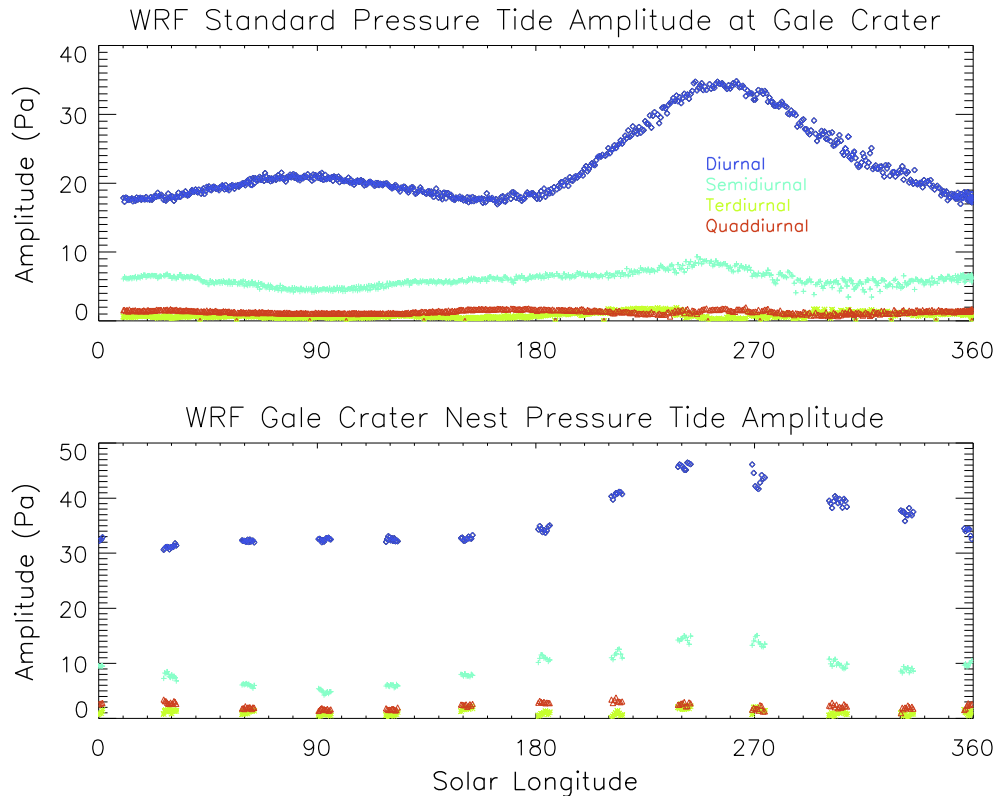
WRF Standard Pressure Tide Amplitude at Gale Crater

WRF Gale Crater Nest Pressure Tide Amplitude

Fig. 7. Diurnal (blue), semidiurnal (light blue), terdiurnal (green) and quadiurnal (orange) tide amplitudes in Pa from the standard 2° × 2° MarsWRF simulation for the grid point nearest to Gale Crater (top) and the same values plotted for the grid point nearest to Bradbury Landing in Gale Crater in the nested simulation (bottom). (For interpretation of the references to color in this figure legend, the reader is referred to the web version of this article.)

Table 1
MarsWRF simulation parameters.

Simulation	Local storm site	Local storm size (grid boxes)
Baseline	N/A	N/A
R1	2.5°S, 137.5°E	1
R2	12.5°N, 292.5°E	1
R3	2.5°S, 137.5°E	9
R4	2.5°S, 137.5°E	25

Database "MGS Scenario" dust prescription (Montmessin et al., 2004; Toigo et al., 2012). The interaction of the migrating diurnal tide (DW1) with the zonal wavenumber 2 component of the topography (also surface thermal inertia, albedo, and spatial distributions of dust) is what generates the eastward-propagating diurnal Kelvin wave (DE1) (Wilson and Hamilton, 1996; Forbes et al., 2002; Guzewich et al., 2012). These two tides interfere with each other, producing the wavenumber 2 pattern of amplitude in longitude. Leovy and Zurek (1979) suggested that destructive interference of the diurnal Kelvin wave and the migrating diurnal tide could account for the rapid dip in diurnal tide amplitude at VL1 at the initiation of the 1977 global dust storm. This was largely confirmed by Wilson and Hamilton (1996) using a GCM simulation. Near Gale Crater (just left of center on each plot), the migrating diurnal tide and diurnal Kelvin wave constructively interfere, producing larger-than-average diurnal tide amplitudes. This fact combined with MSL's low altitude within Gale Crater is what drives the very large diurnal tide amplitudes observed by REMS. Near the Tharsis region and Syrtis Major, the two tides destructively interfere, leading to weaker-than-average diurnal tide amplitudes. Similarly, the semidiurnal tide's amplitude exhibits a wavenumber 4 structure in longitude, indicating interference between the westward-propagating migrating semidiurnal tide

(SW2) and the eastward-propagating non-migrating semidiurnal tide (SE2). In this case, Gale Crater sits in a region of slightly weaker-than-average semidiurnal tide amplitudes. These interference patterns vary with season, as seen in Fig. 6, as the non-migrating tides and migrating tides have different seasonal cycles. For example, the diurnal Kelvin wave is strongest in the solstice seasons (near $L_s = 90°$), while the migrating diurnal tide is strengthened at the equinoxes ($L_s = 180°$). This can also be seen in Fig. 6.

The simulated migrating (DW1 and SW2) tide phases indicated by our standard MarsWRF simulation provide close matches for the diurnal and semidiurnal tide phases, respectively, observed by REMS at Gale Crater (Fig. 6), with a phase near 0500 for the migrating diurnal tide and near 0945 for the migrating semidiurnal tide. This indicates that the eastward-propagating diurnal Kelvin wave (DE1) has little impact on the observed phase of the diurnal tide in Gale Crater, despite the simulation suggesting DE1 has an amplitude approximately 2/3rds the size of DW1 (Fig. 6). This is true despite the interference pattern in longitude strongly implying that DE1 is contributing to the large diurnal tide amplitudes in Gale Crater. DE1's phase in the MarsWRF simulations is quite close to that shown by Wilson and Hamilton (1996), who showed that DE1 could have little impact on the observed phase of the diurnal tide at Gale Crater's longitude, despite having a significant impact on the diurnal tide amplitude (see Fig. 12 of Wilson and Hamilton, 1996). Similarly, Gale Crater's longitude results in SE2 having little influence on the observed semidiurnal tide phase (Wilson and Hamilton, 1996).

When zonally averaged, the amplitude is muted relative to what's observed in Gale Crater. Much of this discrepancy is explained by the low altitude of MSL in Gale Crater that is not fully resolved in a 2° × 2° simulation and that is demonstrated in Fig. 7.
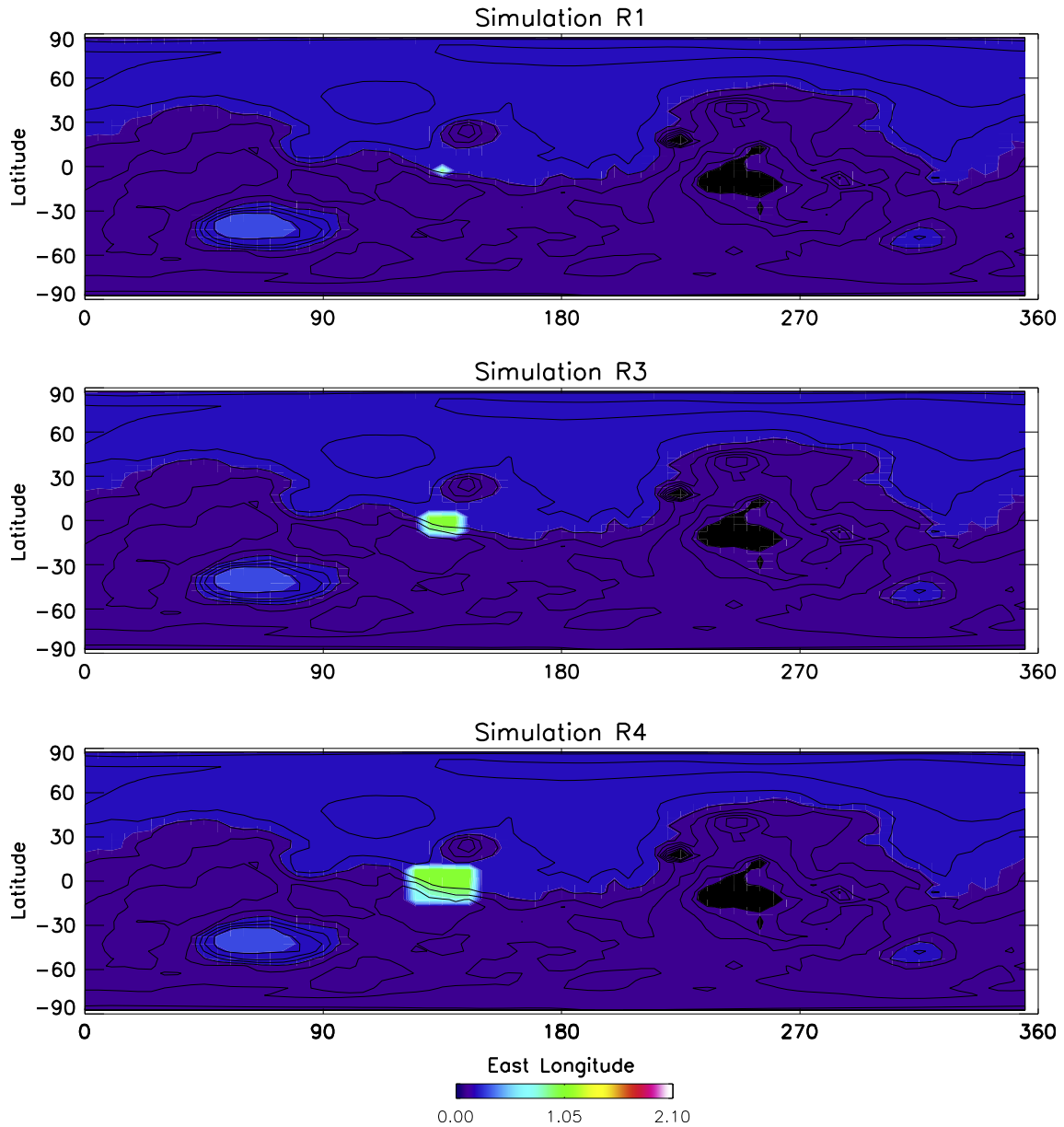
Fig. 8. MarsWRF dust opacity for Simulation R1 (top), Simulation R3 (middle), and Simulation R4 (bottom).

The standard WRF simulation (using the grid points closest to Gale Crater) shows diurnal tide amplitudes of 18–20 Pa that increase to near 35 Pa near northern winter solstice (Fig. 7, top). But, in our simulation using a "nested" high spatial resolution grid box centered over Gale Crater, the maximum diurnal tide amplitude is 47 Pa. These model values can be compared to observed REMS diurnal tide amplitudes of 26–63 Pa (Figs. 1 and 3).

Based on our analysis of tide phase in the MarsWRF simulation, we cannot distinguish the contribution of non-migrating tides to the diurnal and semidiurnal tides observed by REMS. However, the global pattern of diurnal and semidiurnal tide amplitudes suggest that DE1 is helping to strengthen the diurnal tide within Gale Crater while SE2 is slightly weakening the semidiurnal tide.

6. Tide response to a local dust storm

If the atmospheric opacity in Gale Crater is largely representative of global atmospheric aerosol loading (as it, by-in-large, appears to be per Section 4), then based on tidal theory, we would expect the diurnal and semidiurnal tides to respond similarly. As Fig. 4 demonstrates, the high correlations between observed opacity and tide amplitudes indicate that this is precisely what has happened for most of MY31–32. One interesting exception is the local dust storm that impacted Gale Crater near MY32 L_s = 260° and can be seen in Fig. 1 as the brief spike in diurnal tide amplitude and Fig. 3 as a single point of higher opacity amid a downward trend. As described by Malin et al. (2015), a local dust storm formed in western Elysium Planitia and tracked southeastward. New dust lifting within the storm appeared to cease before reaching Gale Crater, but the storm still briefly elevated the atmospheric opacity there. The diurnal tide immediately responded to this local enhancement of atmospheric opacity, increasing in amplitude by approximately 15% from near 45 Pa to 52 Pa on sol 853. However, as this local storm had a negligible impact to the global average atmospheric opacity, the semidiurnal tide exhibits no response and continues its near-linear decline after the MY32 L_s = 220° flushing dust events. As Leovy and Zurek (1979), Wilson and Hamilton (1996), and many others have noted, the meridionally-
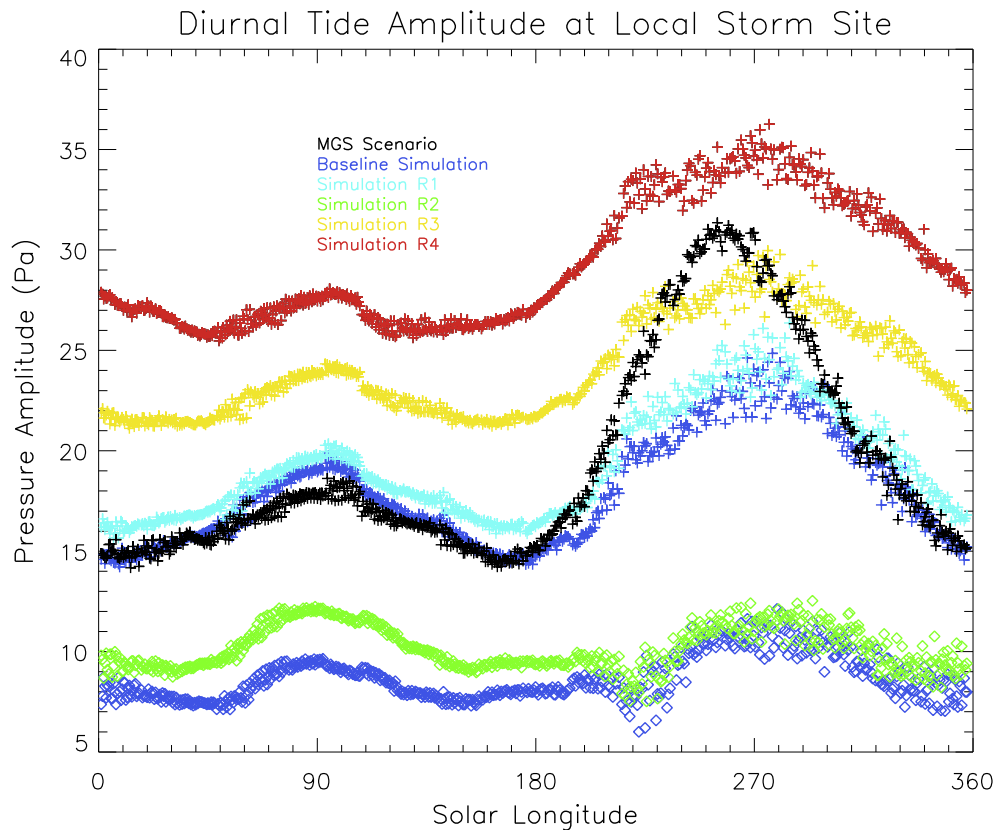
Fig. 9. Diurnal tide amplitude (Pa) through the year for the baseline simulation (blue), Simulation R1 (light blue), Simulation R2 (green), Simulation R3 (yellow), Simulation R4 (red), and the 2° × 2° MarsWRF simulation using the MGS dust scenario (black). Crosses are for tide amplitudes at [2.5°S, 137.5°E] (near Gale Crater) and diamonds for [12.5°N, 292.5°E] (the grid point of the local dust storm in Simulation R2). (For interpretation of the references to color in this figure legend, the reader is referred to the web version of this article.)

broad Hough function and long vertical wavelength of the gravest symmetric mode of the semidiurnal tide make it efficiently excited by increasing global atmospheric aerosol loading and a deep vertical column of aerosol heating. The semidiurnal tide was greatly enhanced during the global dust storms observed by the Viking landers (Leovy and Zurek, 1979; Wilson and Hamilton, 1996) and REMS has observed the semidiurnal tide response to several large regional dust storms. In contrast, the gravest Hough function contribution to the tropical diurnal pressure tide is equatorially-trapped with a much shorter vertical wavelength. Hence it is more sensitive to precisely where the aerosol heating is occurring within the vertical column and to local opacity changes.

Still, little work has been done to quantify the extent of the horizontal range where the diurnal tide is sensitive to localized dust forcing. We conducted a series of MarsWRF simulations to examine this question and these are listed in Table 1. All simulations were at 5° × 5° horizontal resolution. Our baseline simulation had a consistent low atmospheric dust loading that was only scaled to the local surface pressure, thus has a slight seasonal opacity variation that is completely tied to the annual CO_2 cycle. All other simulations shared this global dust loading, but with localized perturbations representing dust storms at various scales and locations and all simulations used a modified Conrath-ν vertical dust profile with a seasonally and latitudinally-variable Conrath parameter as per the "MGS Scenario" (the annual and global average Conrath parameter corresponds to a "top of the dust layer" at 48 km). In Simulation R1, we imposed a "local dust storm" (with dust opacity ∼5 times larger than the surrounding atmosphere) in only the grid box including Gale Crater. In Simulation R2, we imposed an identical dust storm, but in a different location (12.5°N, 292.5°E or approximately 155°E and 15°N of Gale Crater). In Simulations R3

and R4, we returned to the Gale Crater area, but had "local" dust storms covering 3 × 3 or 5 × 5 grid boxes (i.e., covering a 15° × 15° or 25° × 25° region), respectively. Fig. 8 shows the global dust opacity for Simulations R1, R3, and R4. The baseline simulation was identical to the other simulations, except with the imposed dust storms removed.

As expected, the diurnal tide observed at the central grid point of the "local" dust storms sees a clear response from the localized increased dust opacity relative to the baseline simulation. Indeed, in all simulations, the greatest enhancement of diurnal tide amplitude reliably occurs at the central grid point of the imposed local dust storm. The amount of diurnal tide ($S_1(p)$) amplitude increase produced varies seasonally as seen in Fig. 9. For Simulation R1, which is the idealized scenario that most closely represents the local storm impacting Gale Crater in MY32, the simulated local dust storm produces a 7% increase (on an annual-average basis) in diurnal tide amplitude, which (when accounting for the coarse topography in the 5° × 5° simulation) is comparable to the approximately 15% increase actually seen by REMS. Simulations R2, R3, and R4 have annual-average diurnal tide amplitude increases of 19%, 35%, and 64%, respectively, at their local storm sites. Interestingly, for Simulations R1, R3, and R4, where the size of the local dust storm increases from 1 × 1, to 3 × 3, and then 5 × 5 grid points, the tide amplitude increases at the storm's central grid point are roughly linear. When replacing Simulation R1 with Simulation R2 (which is not at the same location as Simulations R3 and R4), the linear fit in size vs. diurnal tide amplitude becomes almost perfect.

Although the amplitudes in all simulations are nearly the highest of the year at $L_s = 260°$ (which coincidentally is the time of year at which the local storm was actually observed at Gale Crater), the
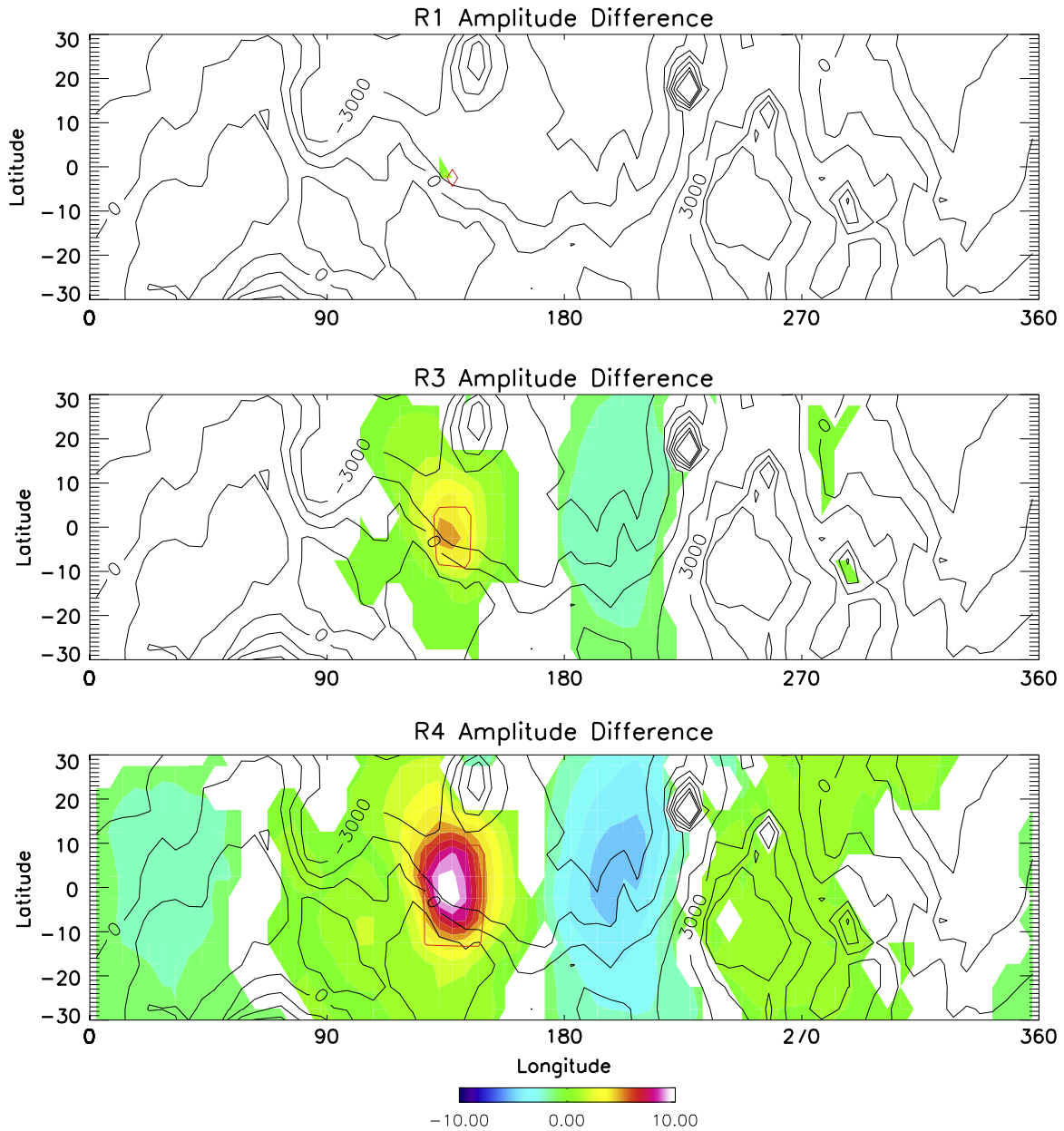
Fig. 10. Difference in diurnal tide amplitude (Pa) from the baseline simulation for Simulation R1 (top), Simulation R3 (middle), and Simulation R4 (bottom) with overlaid topography contours (m). The areas of the imposed local dust storms are indicated by the red contours. (For interpretation of the references to color in this figure legend, the reader is referred to the web version of this article.)

relative change between the baseline simulation and local dust storm Simulations R1, R3, and R4 is minimized near the solstices. This can be seen visually in Fig. 9 (and Fig. 7), where the simulated tide amplitude has a wavenumber 2 structure in solar longitude with peaks at the solstices. The peaks in tide amplitude near Gale Crater are most likely due to the amplified presence of Kelvin waves that are strongest in the two solstice seasons. At the equinoxes, the relative change in amplitude is larger between the baseline and Simulations R1, R3 and R4. This pattern, where the local dust storms are more effective at increasing diurnal tide amplitude at the equinoxes, makes sense. Our local storm has been placed (roughly) at the location of Gale Crater, very near the equator in Simulations R1, R3, and R4. At the equinoxes, the Sun is directly overhead and thus the thermotidal forcing from dust is stronger. The thermotidal forcing is most likely to enhance the migrating tides, which dominate the local response. The Kelvin waves, which

are more prominent in the solstice seasons, are relatively insensitive to dust (e.g., Wilson and Hamilton, 1996). The pattern of Simulation R2 (green symbols in Fig. 10) is different given its location north of the equator (12.5°N). There the thermotidal forcing is enhanced near $L_s = 90°$ and actually maximizes near $L_s = 70°$, when the local storm site is near the sub-solar latitude.

We investigated the change in diurnal tide amplitudes between the baseline simulations and the local storm simulations to determine which particular Hough modes are amplified by the imposed dust storms. We found that indeed the gravest symmetric vertically-propagating Hough mode of the migrating diurnal tide is most clearly amplified by the increased dust loading at the location of the dust storm. Additionally, there is a clear non-local response at high latitudes to the imposed equatorial dust storm that we attribute to the symmetric vertically-trapped Hough modes. The gravest symmetric vertically-trapped Hough mode is

meridionally broad and peaks in amplitude near 50° latitude in both hemispheres (Chapman and Lindzen, 1970).

In Fig. 10 we directly plot the horizontal response of the atmosphere to local dust storms. For the two smallest storms (Simulations R1 and R2), only a small region immediately near the local storm has a diurnal tide enhancement ≥0.5 Pa (corresponding to a 3–5% enhancement of diurnal tide amplitude over the baseline simulation), while the central grid point of each storm has enhancements of 1.2 Pa and 1.6 Pa, respectively. Outside of this small region immediately underneath or surrounding the local dust storm, the diurnal tide has no notable response. In Simulations R3 and R4, the response of the atmosphere is decidedly more regional. In both cases, the largest response, of 6 Pa and 11.1 Pa, respectively, is again at the central grid point of the imposed dust storm. But the region with a diurnal tide enhancement of ≥0.5 Pa is much larger than that seen in Simulation R1 and is much broader in both latitude and longitude (approximately 50° for both) than the local dust storm that is forcing the diurnal tide changes (15° in latitude and longitude). Additionally, there is a weakening of the diurnal tide for a large region directly east of the storm location. This is even more apparent for Simulation R4 where a clear wavenumber 2 pattern in longitude is present around the planet in response to the largest "local" dust storm (perhaps more appropriately now called a "regional" dust storm as it covers 1.5% of the planet's surface area). In Simulation R4, much of the planet's tropics see either an enhancement or weakening of the diurnal tide. As Moudden and Forbes (2008) and Guzewich et al. (2014) describe, the zonal wave 1 modulation (the large local dust storm imposed in the simulation) of the migrating diurnal tide contributes to a diurnal period westward-propagating zonal wavenumber 2 tide. Strikingly, the planetary area experiencing a diurnal tide response (≥0.5 Pa absolute change in diurnal tide amplitude) again scales almost perfectly linearly with the areal size of the imposed dust storm.

7. Conclusions

In this paper we have presented an analysis of REMS observations of atmospheric pressure tides in Gale Crater, linked the observed tide variability to observed local and global dust opacity, and supported our analysis with the MarsWRF GCM. Additionally, we've conducted a GCM study of how the diurnal tide responds to local dust storms.

The diurnal and semidiurnal tides measured in Gale Crater by the REMS pressure sensor are highly correlated (∼0.9) to the local atmospheric opacity observed by MastCam through the first 875 sols of the MSL mission, while the terdiurnal and quadiurnal tides exhibit no correlation and a slight anti-correlation, respectively. The phases of the diurnal, semidiurnal, and quadiurnal tides are generally steady throughout the year, with noticeable phase excursions occurring during large dust events (e.g., the large post-landing regional dust storm near MY31 $L_s = 210°$). The diurnal and semidiurnal tide's average phases are 0424 h and 0929 h, respectively.

With the support of MarsWRF GCM simulations, we find that the migrating diurnal and migrating semidiurnal tides are the predominant contributors to the features of the diurnal and semidiurnal tides observed by REMS, respectively. There is no clear period in the REMS record with an identifiable contribution from a particular non-migrating tide (e.g., the diurnal Kelvin wave) based on phase progression alone. However, the large amplitude of the diurnal tide locally within Gale Crater is due to both the enhancement associated with the low topographic altitude of MSL within Gale Crater and the regional enhancement of the diurnal tide caused by the global pattern of interference between the westward-propagating migrating diurnal tide and the eastward-propagating diurnal Kelvin wave.

Gale Crater experienced a decaying local dust storm late in MY32, causing the diurnal tide amplitude to briefly spike in concert with local dust opacity, while the semidiurnal tide was unresponsive. Using MarsWRF, we conducted a suite of simulations with an imposed local dust storm of varying size and location. We find that the diurnal tide amplitude beneath the center of the local storm consistently experiences the largest increase in amplitude compared to a baseline simulation and that this diurnal tide amplitude enhancement behaves nearly linearly with increasing local dust storm size. Similarly, the size of the region experiencing changes to diurnal tide amplitude scales linearly with increasing storm size. Indeed, when the dust storm approaches a regional scale (as in Simulation R4), most tropical locations experience either an increase or decrease in diurnal tide amplitude.

References

Allison, M., McEwen, M., 2000. A post-Pathfinder evaluation of areocentric solar coordinates with improved timing recipes for Mars seasonal/diurnal climate studies. Planet. Space Sci. 48, 215–235.

Bridger, A.F.C., Murphy, J.R., 1998. Mars' surface pressure tides and their behavior during global dust storms. J. Geophys. Res. 103 (E4), 8587–8601. http://dx.doi.org/10.1029/98JE00242.

Chapman, S., Lindzen, R.S., 1970. Atmospheric Tides. D. Reidel, Norwell, MA.

Clancy, R.T. et al., 2000. An intercomparison of ground-based millimeter, MGS TES, and Viking atmospheric temperature measurements: Seasonal and interannual variability of temperatures and dust loading in the global Mars atmosphere. J. Geophys. Res. 105 (E4), 9553–9571. http://dx.doi.org/10.1029/1999JE001089.

Forbes, J.M. et al., 2002. Nonmigrating tides in the thermosphere of Mars. J. Geophys. Res. 107 (E11), 5113. http://dx.doi.org/10.1029/2001JE001582.

Gómez-Elvira, J. et al., 2012. REMS: The environmental sensor suite for the Mars Science Laboratory. Space Sci. Rev. 170, 583–640.

Gómez-Elvira, J. et al., 2014. Curiosity's Rover Environmental Monitoring Station: Overview of the first 100 sols. J. Geophys. Res.: Planets 119, 1680–1688. http://dx.doi.org/10.1002/2013JE004576.

Guzewich, S.D., Talaat, E.R., Waugh, D.W., 2012. Observations of planetary waves and nonmigrating tides by the Mars Climate Sounder. J. Geophys. Res. 117, E03010. http://dx.doi.org/10.1029/2011JE003924.

Guzewich, S.D. et al., 2013. The impact of a realistic vertical dust distribution on the simulation of the Martian General Circulation. J. Geophys. Res.: Planets 118, 980–993. http://dx.doi.org/10.1002/jgre.20084.

Guzewich, S.D. et al., 2014. Thermal tides during the 2001 martian global-scale dust storm. J. Geophys. Res.: Planets 119, 506–519. http://dx.doi.org/10.1002/2013JE004502.

Guzewich, S.D. et al., 2015. Mars Orbiter Camera climatology of textured dust storms. Icarus 258, 1–13. http://dx.doi.org/10.1016/j.icarus.2015.06.023.

Haberle, R.M., Leovy, C.B., Pollack, J.M., 1982. Some effects of global dust storms on the atmospheric circulation of Mars. Icarus 50, 322–367. http://dx.doi.org/10.1016/0019-1035(82)90129-4.

Haberle, R.M. et al., 2014. Preliminary interpretation of the REMS pressure data from the first 100 sols of the MSL mission. J. Geophys. Res.: Planets 119, 440–453. http://dx.doi.org/10.1002/2013JE004488.

Hamilton, V.E. et al., 2014. Observations and preliminary science results from the first 100 sols of MSL Rover Environmental Monitoring Station ground temperature sensor measurements at Gale Crater. J. Geophys. Res.: Planets 119, 745–770. http://dx.doi.org/10.1002/2013JE004520.

Harri, A.-M. et al., 2014. Pressure observations by the Curiosity rover: Initial results. J. Geophys. Res.: Planets 119, 82–92. http://dx.doi.org/10.1002/2013JE004423.

Kahanpää, H. et al., 2015. Convective vortices and dust devils at the MSL landing site: Annual variability. J. Geophys. Res.: Planets, submitted for publication.

Kleinböhl, A. et al., 2013. The semidiurnal tide in the middle atmosphere of Mars. Geophys. Res. Lett. 40, 1952–1959. http://dx.doi.org/10.1002/grl.50497.

Lemmon, M.T. et al., 2015. Dust aerosol, clouds and the atmospheric optical depth record over 5 Mars years of the Mars Exploration Rover mission. Icarus 251, 96–111. http://dx.doi.org/10.1016/j.icarus.2014.03.029.

Leovy, C.B., 1981. Observations of martian tides over two annual cycles. J. Atmos. Sci. 38, 30–39. http://dx.doi.org/10.1175/1520-0469(1981)038<0030:OOMTOT>2.0.CO;2.

Leovy, C.B., Zurek, R.W., 1979. Thermal tides and martian dust storms: Direct evidence for coupling. J. Geophys. Res. 84 (B6), 2956–2968. http://dx.doi.org/10.1029/JB084iB06p02956.

Lewis, S.R., Barker, P.R., 2005. Atmospheric tides in a Mars general circulation model with data assimilation. Adv. Space Res. 36 (11), 2162–2168.

Malin, M.C., Cantor, B.A., Kennedy, M.R., 2012. MRO MARCIWeather Report for the Week of 12 November 2012–18 November 2012, Malin Space Science Systems Captioned Image Release, MSSS-249. <http://www.msss.com/msss_images/2012/11/21/>.

Malin, M.C. et al., 2013. MRO MARCI Weather Report for the Week of 6 May 2013–12 May 2013, Malin Space Science Systems Captioned Image Release, MSSS-273. <http://www.msss.com/msss_images/2013/05/15/>.

Malin, M.C. et al., 2014a. MRO MARCI Weather Report for the Week of 30 June 2014–6 July 2014, Malin Space Science Systems Captioned Image Release, MSSS-333. <http://www.msss.com/msss_images/2014/07/09/>.

Malin, M.C. et al., 2014b. MRO MARCI Weather Report for the Week of 7 July 2014–13 July 2014, Malin Space Science Systems Captioned Image Release, MSSS-334. <http://www.msss.com/msss_images/2014/07/16/>.

Malin, M.C. et al., 2014c. MRO MARCI Weather Report for the Week of 14 July 2014–20 July 2014, Malin Space Science Systems Captioned Image Release, MSSS-335. <http://www.msss.com/msss_images/2014/07/23/>.

Malin, M.C. et al., 2015. MRO MARCI Weather Report for the Week of 29 December 2014–4 January 2015, Malin Space Science Systems Captioned Image Release, MSSS-358. <http://www.msss.com/msss_images/2015/01/07/>.

Martínez, G.M. et al., 2014. Surface energy budget and thermal inertia at Gale Crater: Calculations from ground-based measurements. J. Geophys. Res.: Planets. http://dx.doi.org/10.1002/2014JE004618.

Martín-Torres, F.J. et al., 2015. Transient liquid water and water activity at Gale Crater on Mars. Nat. Geosci. 8, 357–361. http://dx.doi.org/10.1038/ngeo2412.

Mischna, M.A., Lee, C., Richardson, M., 2012. Development of a fast, accurate radiative transfer model for the martian atmosphere, past and present. J. Geophys. Res. 117, E10009. http://dx.doi.org/10.1029/2012JE004110.

Montmessin, F. et al., 2004. Origin and role of water ice clouds in the martian water cycle as inferred from a general circulation model. J. Geophys. Res. 109, E10004. http://dx.doi.org/10.1029/2004JE002284.

Moores, J.E. et al., 2015. Atmospheric movies acquired at the Mars Science Laboratory landing site: Cloud morphology, frequency and significance to the Gale Crater water cycle and Phoenix mission results. Adv. Space Res. 55, 2217–2238.

Moudden, Y., Forbes, J.M., 2008. Topographic connections with density waves in Mars' aerobraking regime. J. Geophys. Res. 113, E11009. http://dx.doi.org/10.1029/2008JE003107.

Newman, C.E. et al., 2002a. Modeling the martian dust cycle: 1. Representations of dust transport processes. J. Geophys. Res. 107 (E12), 5123. http://dx.doi.org/10.1029/2002JE001910.

Newman, C.E. et al., 2002b. Modeling the martian dust cycle: 2. Multiannual radiatively active dust transport simulations. J. Geophys. Res. 107 (E12), 5124. http://dx.doi.org/10.1029/2002JE001920.

Richardson, M.I., Toigo, A.D., Newman, C.E., 2007. PlanetWRF: A general purpose, local to global numerical model for planetary atmospheric and climate dynamics. J. Geophys. Res. 112 (E09001), 2006J. http://dx.doi.org/10.1029/E002825.

Smith, M.D., 2004. Interannual variability in TES atmospheric observations of Mars during 1999–2003. Icarus 167, 148–165. http://dx.doi.org/10.1016/j.icarus.2003.09.010.

Smith, M.D. et al., 2003. Thermal Emission Imaging System (THEMIS) infrared observations of atmospheric dust and water ice cloud optical depth. J. Geophys. Res. 108, 5115. http://dx.doi.org/10.1029/2003JE002115, E11.

Tillman, J.E. et al., 1993. The martian annual atmospheric pressure cycle: Years without great dust storms. J. Geophys. Res. 98 (E6), 10963–10971. http://dx.doi.org/10.1029/93JE01084.

Toigo, A. et al., 2012. The impact of resolution on the dynamics of the martian global atmosphere: Varying resolution studies with the MarsWRF GCM. Icarus 221 (1), 276–288. http://dx.doi.org/10.1016/j.icarus.2012.07.020.

Wang, H. et al., 2003. Cyclones, tides, and the origin of major dust storms on Mars. Geophys. Res. Lett. 30 (9), 1488. http://dx.doi.org/10.1029/2002GL016828.

Wilson, R.J., 1997. A general circulation model simulation of the martian polar warming. Geophys. Res. Lett. 24 (2), 123–126. http://dx.doi.org/10.1029/96GL03814.

Wilson, R.J., Guzewich, S.D., 2014. Influence of water ice clouds on nighttime tropical temperature structure as seen by the Mars Climate Sounder. Geophys. Res. Lett. 41, 3375–3381. http://dx.doi.org/10.1002/2014GL060086.

Wilson, R.J., Hamilton, K., 1996. Comprehensive model simulation of thermal tides in the martian atmosphere. J. Atmos. Sci. 53, 1290–1326. http://dx.doi.org/10.1175/1520-0469(1996)053<1290:CMSOTT>2.0.CO;2.

Wilson, R.J., Lewis, S.R., Montabone, L., 2008. Influence of water ice clouds on martian tropical atmospheric temperatures. Geophys. Res. Lett. 35, L07202. http://dx.doi.org/10.1029/2007GL032405.

Wilson, R.J. et al., 2014. GCM simulations of aphelion season tropical cloud and temperature structure. In: Mars Atmosphere: Modeling and Observations, 5th International Workshop, Oxford, UK. <http://www-mars.lmd.jussieu.fr/oxford2014/abstracts/wilson_clouds_oxford2014.pdf>.

Zurek, R.W., 1980. Surface pressure response to elevated tidal heating sources: Comparison of Earth and Mars. J. Atmos. Sci. 37, 1132–1136. http://dx.doi.org/10.1175/1520-0469(1980)037<1132:SPRTET>2.0.CO;2.

Zurek, R., Leovy, C.B., 1981. Thermal tides in the dusty martian atmosphere: A verification of theory. Science 213, 437–439. http://dx.doi.org/10.1126/science.213.4506.437.